

# Neon retention in tungsten, boron and mixed thin-films under the effects of thermal annealing studied by isotopic tracing<sup>☆</sup>

D.N. Gautam<sup>a,\*</sup> , D. Primetzhofer<sup>a</sup>, M. Rubel<sup>a,b</sup> , E. Pitthan<sup>a</sup> 

<sup>a</sup> Department of Physics and Astronomy, Ångström Laboratory, Uppsala University, Box 516, SE-751 20 Uppsala, Sweden

<sup>b</sup> KTH Royal Institute of Technology, Department of Electromagnetic Engineering and Fusion Physics, 100 44 Stockholm, Sweden

## ABSTRACT

The retention of two neon isotopes, <sup>20</sup>Ne and <sup>22</sup>Ne, was studied by ion beam analysis (IBA) for thin-films of mixed W and B as well as for pure W and B layers grown on silicon-and tungsten-substrates by means of magnetron sputter deposition. Each isotope was implanted to a fluence of  $3 \times 10^{16}$  at./cm<sup>2</sup> but at different energies (35–190 keV) to obtain deposition profiles closer to the surface and deeper into the film, depending on isotope and thin-film composition. Thermal annealing in combination with IBA was used to investigate the Ne-retention in a range of temperatures between RT and 1000 °C. Time-of-flight elastic recoil detection analysis was employed to monitor the retention and depth profiles of the Ne isotopes. Both Ne-isotopes remain at their original implantation depth, thus not indicating diffusion, intermixing or desorption for the full range of temperatures and for all studied compositions.

## 1. Introduction

There are several ways in which Ne-seeding is utilized in fusion devices. Puffing of Ne during plasma discharges is used for radiative cooling and reduction of divertor heat loads. It has been beneficial for both enhancing the confinement and lowering the high-confinement mode (H-mode) threshold power [1,2]. Other uses of Ne include disruption mitigation, wall conditioning [3] and application as a tracer element for diagnostics and retention studies [4,5]. The retention of Ne in plasma-facing materials (PFM) has been observed in previous studies [4–7]. Uncontrolled releases of medium-Z impurities such as oxygen (O) and Ne will, however, degrade plasma performance and can lead to erosion of PFM by sputtering of tungsten (W) and other high-Z elements. This would lead to significant radiation losses in the core plasma and can result in plasma disruptions [8,9] which can in turn lead to further erosion [10].

For tokamaks such as ITER with W as the choice for PFM [11–13], wall conditioning will be necessary to improve the start-up phase and the overall plasma performance, which includes gettering of unavoidable oxygen impurities [14,15]. To this end, a boronization process will have to be implemented in ITER [16]. It was developed in 1988 starting at TEXTOR [17] and has since been successfully applied in several other devices [13–22]. An inevitable consequence of boronization in ITER will be the formation of W-B mixtures on the first wall and divertor surfaces due to continuous erosion and re-deposition steps during plasma-wall

interactions. The presence of W-B mixtures have been identified during an ex-situ study of WEST wall components [21]. Ne puffing will result in Ne co-deposition with the W-B mixtures in a reactor [6,7]. This calls for studies to understand and assess the possible impact of Ne retention in B, W and their mixtures on the operation of tokamaks.

This project includes characterization of material properties at elevated temperatures, since surface temperatures of PFM can exceed 600 °C [23–25] in some areas of a reactor. The aim of this work was to determine neon retention in thin films of pure W and B, and W-B mixtures under thermal annealing in a broad thermal range from room temperature (RT) to 1000 °C.

## 2. Materials and methods

### 2.1. Deposition of W-B thin-film layers

A PREVAC magnetron sputtering system was used to grow the pure W, pure B and mixed W-B thin-films [26]. In total, 24 samples were grown, 12 of which were on silicon (Si) < 100 > wafers and 12 on 0.5 mm thick W sheets. The different substrates (Si or W), all approximately 1 cm<sup>2</sup> in size, were ultrasonically cleaned for 10 min in an ethanol bath and individually dried using pressurized air prior to being loaded into the sputtering system. The magnetron system is currently equipped with four MS2 63C1 magnetron sources suitable for targets with 2" diameter and 1–6 mm thickness. In total, three different depositions were

<sup>☆</sup> This article is part of a special issue entitled: 'PWI – J. Roth' published in Nuclear Materials and Energy.

\* Corresponding author.

E-mail address: [daniel.gautam@physics.uu.se](mailto:daniel.gautam@physics.uu.se) (D.N. Gautam).

performed, see Table 1 for more details. Prior to the depositions of the B-layers the substrates were all annealed in-situ in the Load-Lock (LL) system of the sputtering machine. Once a base pressure of  $9 \times 10^{-7}$  mbar was reached, the annealing began and substrates were kept at 1000 °C for 10 min, before being allowed to passively cool down for 30 min and subsequently be transferred from the LL chamber to the sputtering chamber. The general procedure for deposition was the same for all samples, with a minor exception for the B-deposition (discussed at the end of the section), and is described in the following. With base pressures in the sputtering chamber between  $1.9 \times 10^{-7}$  and  $5.5 \times 10^{-7}$  mbar, argon (Ar) was introduced into the chamber to act as sputtering gas during the depositions which were performed at RT at a pressure of  $5.6 \times 10^{-3}$  mbar. When growing the mixed W-B films, two independently controlled magnetrons were used simultaneously to achieve the desired W-to-B ratio. The power supplied to the respective magnetrons depended on the desired film composition. The W-films were grown with a magnetron power of 50 W direct current (DC), while the mixed W-B deposition used instead 20 W radiofrequency (RF) discharges for the W-target and 50 W (RF) to the B-target and lastly, for the B depositions, 150 W (RF) was supplied to the B-target. For all depositions a quartz crystal microbalance (QCM) was used to determine the deposition rate and to estimate the final thickness of the respective films.

For the B-film depositions, which took in total 6 h, there was an interruption in the film-growth after the first 5.2 h, where the films remained in high vacuum overnight before continuing the deposition the following day, depositing again for the remaining 0.8 h. Once the films were exposed to atmosphere, post-deposition, a green opaque coloration was observed on the samples, regardless of substrate type.

## 2.2. Sample characterization and implantation of Ne-isotopes

Following the film depositions the samples were implanted (350 kV Danfysik equipment at Uppsala University [28]) first with  $^{22}\text{Ne}$  and then with  $^{20}\text{Ne}$  at different energies chosen based on SRIM [29] simulations where the film compositions and thicknesses had to be estimated based on results from prior studies [27]. Table 1 details the energies used during each of the six implantations. The reason behind the isotope implantation order stems from the damage that is expected to be introduced in the films during the implantations, which is calculated by SRIM to be significant, also listed in Table 1. The damage per atom (dpa) calculations were done by using the 'quick calculation of damage' option in SRIM with displacement energy thresholds of 19.36 eV for B [30] and 90 eV for W [31]. The higher energy implantations of the heavier isotope that will penetrate the deepest are done first, followed by a shallower implantation, aiming to minimize the disturbance of the implantation profile closer to the surface.

The expected energies of the majority of ions that impact PFM during nominal operation of tokamaks like ITER are on the order of hundreds of eV or less [32], as compared to the tens-to-hundreds of keV implantation energies used in this study. Since the focus of this study was not to

investigate the effects of damage induced by Ne in PFM, the ion energies were chosen to ensure well-separated implantation depth profiles at specific regions (close to the surface and deeper in layer) of the two Ne-isotopes to investigate their mobility in the studied materials.

## 2.3. Annealing steps and ToF-ERDA measurements

One sample of each substrate type from each of the three batches (B, W:B and W) was stored at room temperature (RT) for the duration of the study as a control. The samples were annealed using the same PREVAC system which was used for the sample preparation. Annealing stages exist both in the LL- and deposition chamber of the system and the prior was used to anneal all samples. The samples were annealed three separate times, to different temperatures each time, and were measured by time-of-flight elastic recoil detection analysis (ToF-ERDA) after each annealing step to track the Ne-content and distribution of the individual isotopes in the samples. For the ToF-ERDA analysis of the samples, they were transferred to beamline T4 of the MV NEC-5SDH-2 pelletron tandem accelerator of the Tandem Laboratory (see [28] for further details), where the film compositions and purities of the annealed and non-annealed samples could be determined using a primary beam of 36 MeV  $^{127}\text{I}^{8+}$ . The film densities were found experimentally in a previous study [27], where the same recipe for growing the films was used as in this work. Using the film densities together with the ToF-ERDA measurements allows for calculation of the film thicknesses, listed in Table 1.

The annealed samples were kept at respective target temperature for 1 h in vacuum before being allowed to passively cool down, for a minimum of 30 min to reach close to RT. The base pressures prior to and after the annealing steps were in the range of  $1 \times 10^{-7}$  to  $9.5 \times 10^{-7}$  mbar and a maximum of  $8 \times 10^{-7}$  to  $18 \times 10^{-7}$  mbar during.

In the first annealing step, samples were annealed to either 200 °C, 300 °C or 400 °C. For each temperature, two samples – one grown on Si and one on W – were chosen from each of the three grown batches. This results in six samples per target temperature, or 18 samples that were annealed in total. All samples were then measured by ToF-ERDA following this first annealing step.

In the second step, samples were annealed to either 500 °C, 600 °C or 700 °C. The same 18 samples from the first annealing step were used once again. The six samples that were previously annealed to 200 °C (300 °C and 400 °C) were in the second step brought to 500 °C (600 °C and 700 °C, respectively). Following the second annealing step the annealed samples were measured by ToF-ERDA once again. The samples kept at RT were not included during this measurement.

In the third and last annealing step, samples were treated at 800 °C, 900 °C or 1000 °C. The same 18 samples from the prior annealing steps were used once again. Following the same recipe as for the second annealing step, the samples that were previously annealed to 500 °C (600 °C and 700 °C) were in this step annealed to 800 °C (900 °C and 1000 °C, respectively). Following this final annealing step, all 18 samples were measured once more by ToF-ERDA, together with the six samples kept at RT.

## 3. Results and discussion

### 3.1. Sample pre-characterization and simulation

Prior to implantation of the samples, simulations were made to choose appropriate implantation energies for the different sample compositions and Ne-isotopes. The binary collision approximation model SRIM [29] was used for the simulations and the results can be seen in Fig. 1. While the SRIM code is a good tool for quick estimations, the reader should be made aware that SRIM assumes a static target, meaning that it does not account for the damage done during implantation when calculating the final depth profiles. The program also does not calculate diffusion, saturation, desorption or mobility of implanted species and is known to provide unrealistic results such as

**Table 1**

Ne implantation energies and predicted implantation ranges (the average depth of the implanted ions) are shown. The nominal fluence for each of the six implantations was  $3 \times 10^{16}$  at./cm<sup>2</sup>. The film thicknesses were calculated using the listed experimental densities together with information from the areal densities from ToF-ERDA measurements.

	W	W:B	B
$^{22}\text{Ne}$ impl. energy (keV)	190	150	65
$^{20}\text{Ne}$ impl. energy (keV)	100	90	35
$^{22}\text{Ne}$ impl. range (nm), SRIM	113.4	144.8	109.5
$^{20}\text{Ne}$ impl. range (nm), SRIM	64.1	92.7	62.4
Maximum $^{22}\text{Ne}$ impl. damage (dpa), SRIM	10.5	8.5	11.1
Maximum $^{20}\text{Ne}$ impl. damage (dpa), SRIM	11.0	9.4	12.1
Film density (g/cm <sup>3</sup> ), experimental [27]	18.70	10.00	2.47
Film thickness (nm), calculated	212	179	137

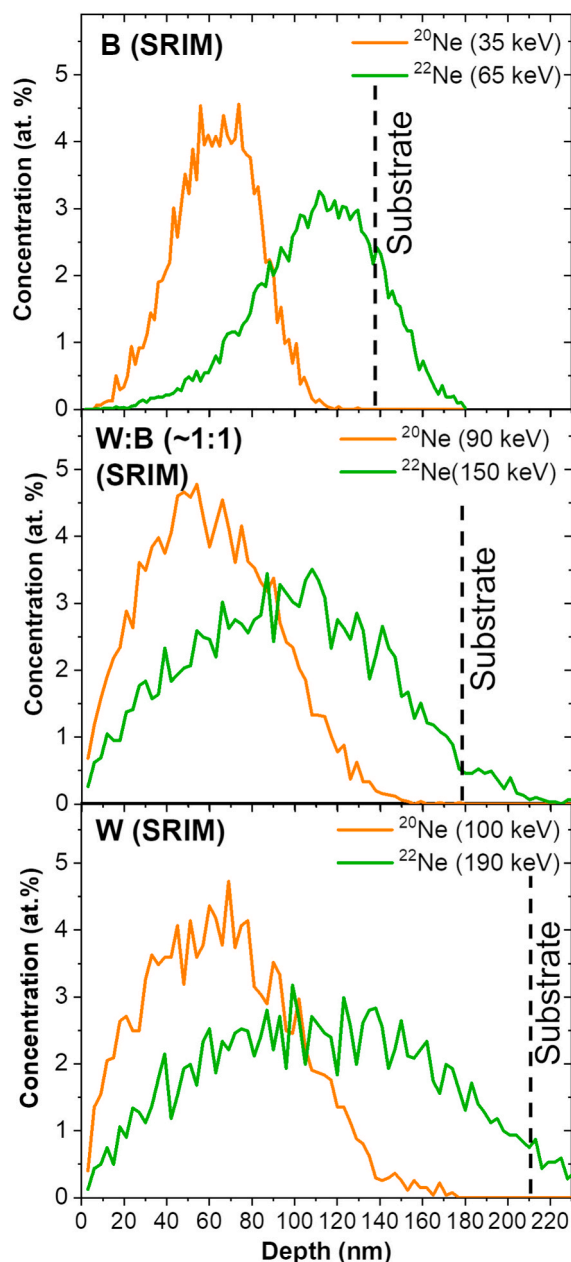


Fig. 1. Composition depth profiles for  $^{20}\text{Ne}$  and  $^{22}\text{Ne}$  implanted in the different film compositions as simulated by SRIM. The film-substrate interfaces were determined from ToF-ERDA measurements of the grown films.

overestimations of vacancies [33] and false distributions of sputtered atoms [34]. The film-substrate interfaces, obtained from later ToF-ERDA measurements of the grown samples and converted to nm-scale based on previous experimentally obtained densities [27], are also indicated in the figure for the B-, W:B- and W-films grown on Si. The implantation energies were chosen to get a good separation of the Ne-isotope profiles.  $^{20}\text{Ne}$  (natural abundance of 90.48 %) implantations were performed at lower energies in comparison to  $^{22}\text{Ne}$  (natural abundance of 9.25 %). By using an isotopic sensitivity technique to investigate the distribution of the different isotopes, the potential interdiffusion between neon implanted at different regions after annealing steps can be traced.

The ToF-ERDA technique allows for elemental and isotopic mass separation in a broad mass range, making it ideal for the samples studied in this work. Fig. 2 shows the raw ToF-ERDA spectrum from one of the measurements. In addition to mass separation, the technique also provides depth information about the detected recoils, allowing for depth

profiling of the analyzed samples.

The raw ToF-ERDA spectra from each measurement were analyzed using the Potku software [35] (version 2.2.5) and converted into atomic fraction depth profiles, see Fig. 3. To calculate the depth profiles 4 iterations were used, with stopping powers values calculated by SRIM as an external subroutine for Potku, and screening corrections by Andersen were chosen for the elemental cross sections. The W/Si sample showed possible signs of W-Si formation after annealing above  $900^\circ\text{C}$ , seen in the depth profiles as a migration of the Si edge towards the film surface accompanied by a lowering of the W edge near the film-substrate interface. This type of change is however also consistent with increased film roughness. W-Si is known in literature to form above  $900^\circ\text{C}$  [36], and was thus expected during the experiments.

The Ne-depth profiles show little to no change throughout the investigated temperature range, as can be seen in Fig. 4. The  $^{22}\text{Ne}$ -implantation of the B/Si samples resulted in a significant portion of the implanted species reaching beyond the film-substrate interface. This was mainly due to the initially aimed thickness, 180 nm, of the films which were in fact closer to 140 nm thick. The same can be said for the W:B-films, although in those cases the effect is not as significant.

The depth resolution and accuracy of atomic concentration measurements in ToF-ERDA can be close to  $\sim 30$  nm at the sample surface [37] but is affected by energy loss straggling and multiple scattering effects, with the effects being stronger at increased depth and in the presence of high-Z elements. Due to limited probing depth for the measurements of the W-films [38] the signal from deeper in the samples (beyond the film-substrate interface) is not analyzed deeper in the layer, as can be seen by the sudden cut-off around  $3 \times 10^{18}$  at./cm $^2$  in the  $^{22}\text{Ne}$  profiles in the figure.

The implanted Ne remains at the depth to which it was implanted, up to the highest temperatures studied in this work. Only after annealing above  $800^\circ\text{C}$  of the W:B/Si is there a significant shift of the Ne-profiles towards the substrate. It is known in literature that Ne-implantation at different energies can lead to the formation of bubbles or dislocation loops [39] as well as other defects in Si [40,41], W [42,43] and other materials [44–46], that can act as trapping sites and which may affect retention. In the  $^{22}\text{Ne}$ -depth profile for the B/Si sample, Fig. 4, it can be seen that a significant amount of the implanted ions was initially trapped by the film-substrate interface region.

The use of keV ions during implantation can affect the Ne-retention, or amount of Ne that is trapped, in the sample. For comparison, in the case of another noble gas, Helium (He), when implanted at 1 MeV, has been observed to remain in W until  $1700^\circ\text{C}$  but started being released at close to RT when implanted at lower energies [47,48]. For high fluence low energy irradiations of He (or Ne), the implantation depth profile will be shallower and more concentrated as compared to irradiations at higher energy. In the former case, there is a higher possibility to reach the saturation limit of the film [49], where He (possibly also in the case of Ne) may be trapped closer to the surface.

Results from literature indicate that the diffusion energy for He in bulk W is significantly lower than that of Ne [50]. This fact might suggest that Ne in W should be less mobile than He at RT, however other relevant factors to consider are e.g. damage caused during irradiation, trapping mechanisms and implantation depths, all of which will be different for the two noble gases.

Fig. 5 shows the Ne-retention in the three studied compositions for the films grown on Si-substrates. No significant differences in Ne-retention were observed between the samples grown on W-substrates (not shown) and Si-substrates. The Ne amounts were obtained by integrating the composition depth profiles calculated by Potku, only considering the Ne in the films and not the substrates, the depths of which are different for each composition, as indicated in Fig. 4. The Ne content was then normalized to the Ne areal densities obtained for the ‘as grown’ samples. For the ToF-ERDA measurements, unknown specific energy losses of detected recoils and uncertainties in detector efficiencies [37], as well as contributions of multiple scattering effects of

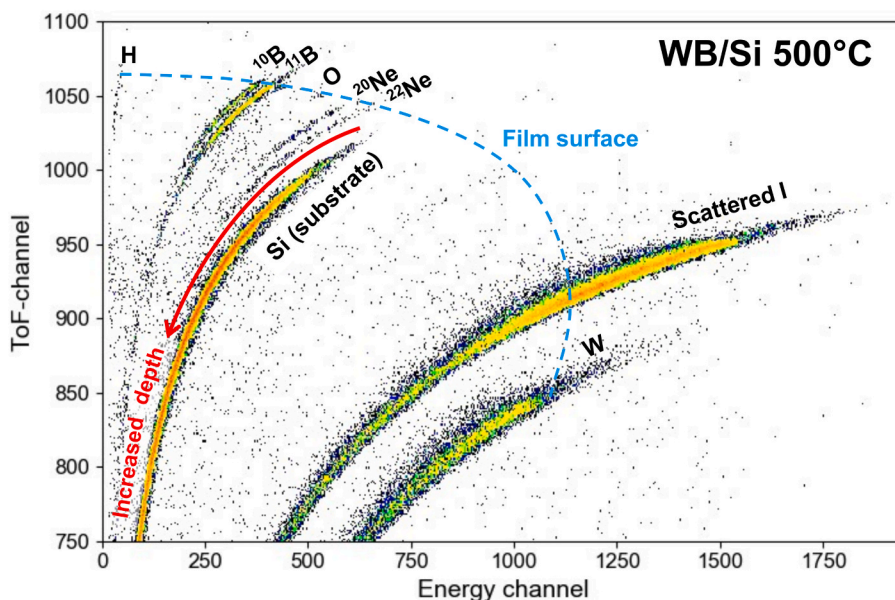


Fig. 2. Example of a ToF-ERDA time-energy coincidence spectrum. The spectrum shows detected signals from the W:B-film grown on Si, with each curved region corresponding to a specific mass which can be identified as elements or isotopes, as is indicated in the figure. The expected signal position from species located at the film's surface is indicated, qualitatively, by the dashed line and signals detected towards the bottom left in the spectrum, indicated by the red arrow, originate from deeper within the sample. The iodine signals are not part of the sample but originate from the incident beam, which is being scattered predominantly by the W in the film. (For interpretation of the references to colour in this figure legend, the reader is referred to the web version of this article.)

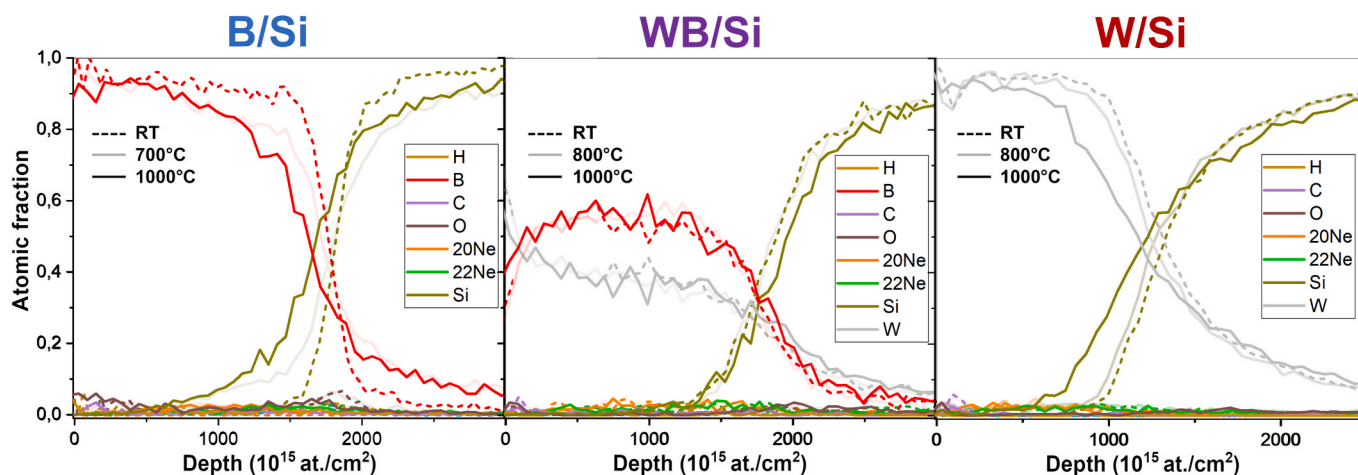


Fig. 3. Composition depth profiles obtained from ToF-ERDA measurements and analyzed using Potku are here shown for three temperatures for each composition.

primary and recoiled species [38] are assumed to introduce systematic uncertainties to the measured Ne-amounts of 10 %. Statistical uncertainties stemming from the detected quantity of each Ne-isotope during the measurements were accounted for in the error estimation and ranged between 3.1–6.8 %. This results in final uncertainties between 10.5–12.1 % for the individual isotopes. In combination, we obtain final uncertainties of the total Ne-amounts around 15.0–16.8 % as seen in Fig. 5. As the specific energy loss is a systematic uncertainty for a given sample system (B, W:B or W), just as detection efficiencies and other experimental parameters are systematic uncertainties for a given run, i.e. measurement day, these uncertainties are valid for a comparison of different samples from different runs, where comparisons within a run and for one system only being more accurate.

Results here indicate that implanted neon, independent of the implantation region, film material, or substrate used, are highly stable as no significant release, diffusion or intermixing between the different isotopes was observed. Within the uncertainties we can expect a loss of,

at most, 30 % of the initially measured total Ne-amount after annealing to 1000 °C (mixed film). These observations are in good agreement with [43] that also observed high stability of Ne in W measured using thermal desorption spectroscopy (TDS) for neon implanted at low energies and annealed up to 1200 °C. In the same publication, a desorption peak was however observed between 700–800 °C, which was not directly observed in this work and which could possibly be attributed to the differences in implantation energies. Slight changes in depth resolution and systematic uncertainties for analysis performed at different days could contribute to the observed fluctuation of the measured Ne-content and are potential reasons for the trends seen in the data.

Here we have shown that for the two isotopes  $^{20}\text{Ne}$  and  $^{22}\text{Ne}$  in W, B and mixed W:B-films implanted at 35–190 keV at fluences of  $3 \times 10^{16}$  at./cm<sup>2</sup>, there was no clear evidence for Ne-desorption for any of the compositions following annealing to several temperatures up to 1000 °C.

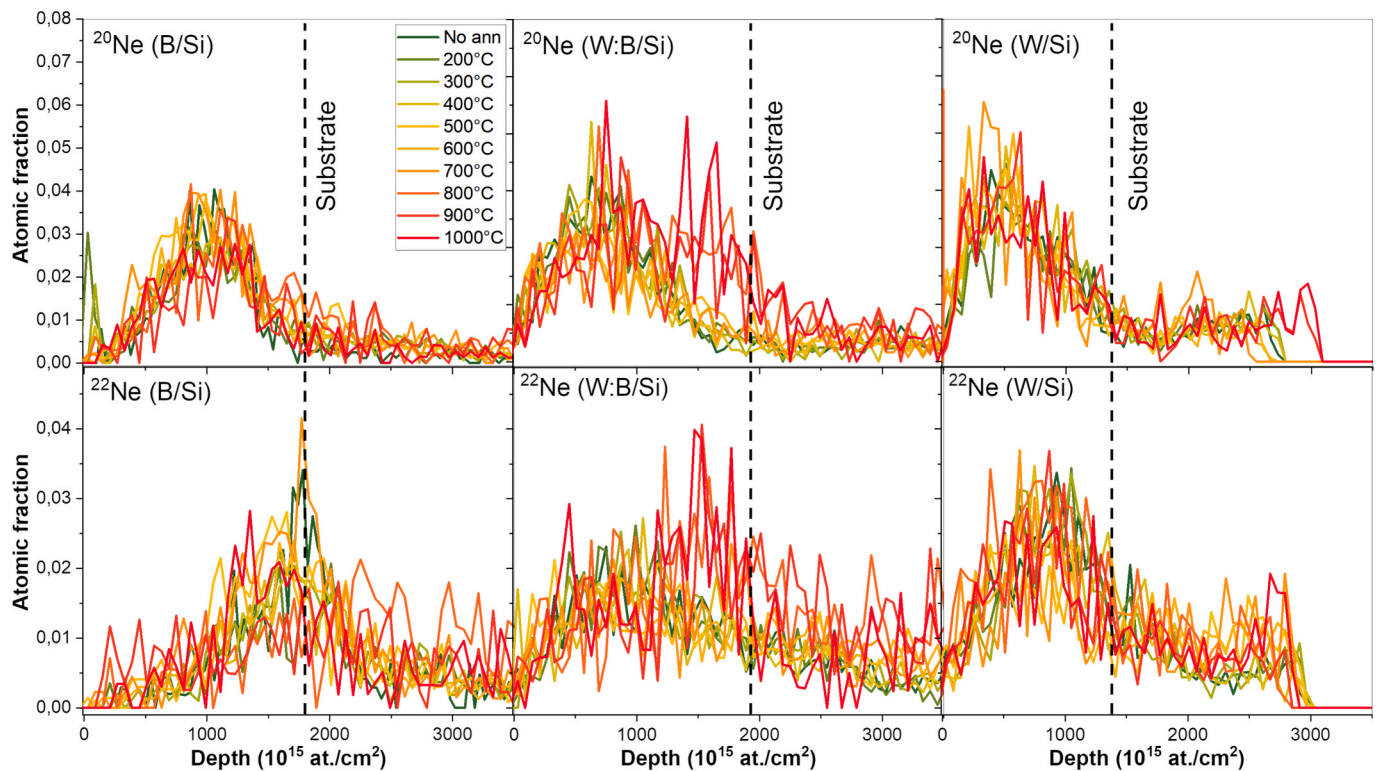


Fig. 4. Composition depth profiles of Ne-isotopes after implantation and the subsequent annealing steps. The film-substrate interfaces are indicated by the dashed lines.

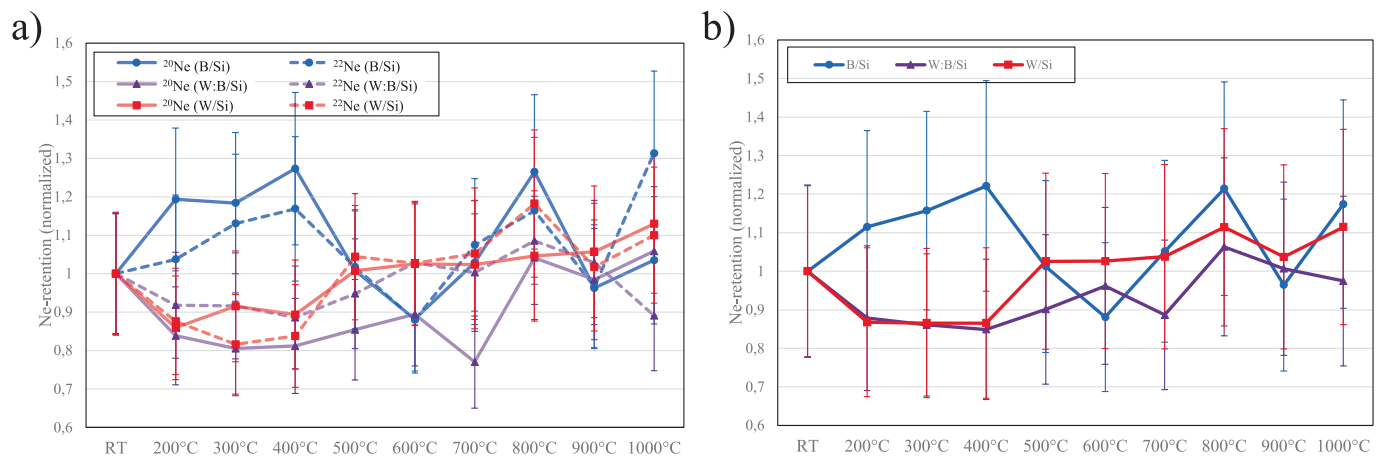


Fig. 5. A) Measured retained Ne-isotopic content, normalized by the retained amounts in the samples kept at RT. B) The total amounts of Ne ( $^{20}\text{Ne} + ^{22}\text{Ne}$ ) for the three studied film compositions, normalized by the total Ne-amounts measured in the samples kept at RT. The data points for the samples kept at RT are average values based on two separate measurements.

#### 4. Concluding remarks

These are the first-ever studies of Ne-retention in thin-films of W, B and their mixtures by implantation of  $^{20}\text{Ne}$  and  $^{22}\text{Ne}$  as isotopic tracers as well as of the behavior of such layers under annealing over a broad range of temperatures. Within the present study, the use of ToF-ERDA as an isotopic tracing technique to study the evolution of Ne concentrations depth-profiles within thin-films is demonstrated to be a viable analysis tool.

This work contributes to the understanding of retention of noble gases in first wall materials of future fusion devices. The depth profiles of  $^{20}\text{Ne}$  and  $^{22}\text{Ne}$  remain unchanged for all samples up to the highest annealing temperature of 1000°C. This observation suggests that Ne

incorporated in such layers is very stable, i.e. little to no mobility is observed. Only for the W:B mixture was a shift of the Ne-profiles observed after annealing to 800 °C, possibly driven by a change in sample chemistry during the formation of W-Si at the film-substrate interface. Follow-up studies will be extended to examine the retention of deuterium in W-B mixtures under a broad range of conditions.

#### CRediT authorship contribution statement

**D.N. Gautam:** Writing – original draft, Visualization, Validation, Methodology, Investigation, Formal analysis. **D. Primetzhofer:** Writing – review & editing, Supervision, Methodology, Funding acquisition, Data curation, Conceptualization. **M. Rubel:** Writing – review & editing,

Conceptualization. E. Pitthan: Writing – review & editing, Supervision, Project administration, Methodology, Investigation, Funding acquisition, Formal analysis, Data curation.

### Declaration of competing interest

The authors declare that they have no known competing financial interests or personal relationships that could have appeared to influence the work reported in this paper.

### Acknowledgements

This work has been carried out within the framework of the EUROfusion Consortium, funded by the European Union via the Euratom Research and Training Programme (Grant Agreement No. 101052200—EUROfusion). Views and opinions expressed are, however, those of the author(s) only and do not necessarily reflect those of the European Union or the European Commission. Neither the European Union nor the European Commission can be held responsible for them. Accelerator operation was supported by the Swedish Research Council VR-RFI, Contract No. 2019\_00191. This work was supported by the Swedish Energy Agency (Grant No. P202301345).

### References

- [1] L.Y. Meng, et al., Divertor plasma behaviors with neon seeding at different locations on EAST with ITER-like divertor, *Nucl. Fusion* 62 (8) (June 2022) 086027, <https://doi.org/10.1088/1741-4326/ac74cf>.
- [2] I. Ivanova-Stanik, R. Zagórski, I. Voitsekhovitch, S. Brezinsek, "Influence of impurity seeding on plasma burning scenarios for ITER," *Proc. 12th Int. Symp. Fusion Nucl. Technol.-12 ISFNT-12*, vol. 109–111, pp. 342–346, Nov. 2016, doi: 10.1016/j.fusengdes.2016.02.102.
- [3] M. Fukumoto, et al., Hydrogen removal by electron cyclotron wall conditioning with neon gas and its impact of tokamak plasma start-up on the QUEST spherical tokamak, *Nucl. Fusion* 64 (6) (May 2024) 066022, <https://doi.org/10.1088/1741-4326/ad3d6e>.
- [4] L. Dittrich, P. Petersson, S. Moon, M. Rubel, T.T. Tran, A. Widdowson, Retention of noble and rare isotope gases in plasma-facing components – Experience from the JET tokamak with the ITER-like wall, *Fusion Eng. Des.* 192 (July 2023) 113620, <https://doi.org/10.1016/j.fusengdes.2023.113620>.
- [5] S. Hou, et al., Development of a multi-spectral extreme ultraviolet imaging diagnostics on the experimental advanced superconducting Tokamak, *Fusion Eng. Des.* 208 (Nov. 2024) 114681, <https://doi.org/10.1016/j.fusengdes.2024.114681>.
- [6] Y.M. Kim, et al., Retention of neon in graphite after ion beam implantation or exposures to the scrape-off layer plasma in the TEXTOR tokamak, *J. Vac. Sci. Technol. A* 20 (1) (Jan. 2002) 138–145, <https://doi.org/10.1116/1.1427890>.
- [7] M. Rubel, V. Philipps, L. Marot, P. Petersson, A. Pospieszczyk, B. Schweer, "Nitrogen and neon retention in plasma-facing materials," *Proc. 19th Int. Conf. Plasma-Surf. Interact. Control. Fusion*, vol. 415, no. 1, Supplement, pp. S223–S226, Aug. 2011, doi: 10.1016/j.jnucmat.2010.08.035.
- [8] E.J. Strait, et al., Progress in disruption prevention for ITER, *Nucl. Fusion* 59 (11) (June 2019) 112012, <https://doi.org/10.1088/1741-4326/ab15de>.
- [9] R.A. Pitts, et al., Plasma-wall interaction impact of the ITER re-baseline, *Nucl. Mater. Energy* 42 (Mar. 2025) 101854, <https://doi.org/10.1016/j.nme.2024.101854>.
- [10] J. Roth et al., "Recent analysis of key plasma wall interactions issues for ITER," *Proc. 18th Int. Conf. Plasma-Surf. Interact. Control. Fusion Device*, vol. 390–391, pp. 1–9, June 2009, doi: 10.1016/j.jnucmat.2009.01.037.
- [11] P. Barabaschi, A. Fossen, A. Loarte, A. Becoulet, L. Coblenz, ITER progresses into new baseline, *Fusion Eng. Des.* 215 (June 2025) 114990, <https://doi.org/10.1016/j.fusengdes.2025.114990>.
- [12] A. Loarte et al., Initial evaluations in support of the new ITER baseline and Research Plan, *Tech. Rep. No ITR-24-004*, 2024.
- [13] J. Bucalossi, et al., WEST full tungsten operation with an ITER grade divertor, *Nucl. Fusion* 64 (11) (Sept. 2024) 112022, <https://doi.org/10.1088/1741-4326/ad64e5>.
- [14] Y.-G. Kim, et al., Effect of impurities in vacuum vessels on the plasma parameters in inductive discharges, *Vacuum* 215 (Sept. 2023) 112330, <https://doi.org/10.1016/j.vacuum.2023.112330>.
- [15] V.A. Shurygin, Light impurities: equilibrium, transport and density profiles in tokamak and stellarator plasmas, *Plasma Phys. Control. Fusion* 65 (10) (Aug. 2023) 105002, <https://doi.org/10.1088/1361-6587/acef90>.
- [16] A. Loarte, et al., The new ITER baseline, research plan and open R&D issues, *Plasma Phys. Control. Fusion* 67 (6) (June 2025) 065023, <https://doi.org/10.1088/1361-6587/add9c9>.
- [17] J. Winter, et al., Boronization in textor, *J. Nucl. Mater.* 162–164 (1989) 713–723, [https://doi.org/10.1016/0022-3115\(89\)90352-8](https://doi.org/10.1016/0022-3115(89)90352-8).
- [18] Y. Yamauchi, et al., Deuterium retention of low activation ferritic steel and boronized wall in JFT-2M, *Fusion Eng. Des.* 81 (1) (2006) 315–319, <https://doi.org/10.1016/j.fusengdes.2005.09.031>.
- [19] S.-H. Hong, et al., First boronization in KSTAR: Experiences on carborane, *J. Nucl. Mater.* 415 (1 Supplement) (2011) S1050–S1053, <https://doi.org/10.1016/j.jnucmat.2010.10.059>.
- [20] V. Rohde, M. Balden, K. Krieger, R. Neu, Boronization with tungsten plasma-facing surfaces in ASDEX Upgrade, *Nucl. Mater. Energy* 43 (June 2025) 101923, <https://doi.org/10.1016/j.nme.2025.101923>.
- [21] A. Marin, et al., XPS post-mortem analysis of plasma-facing units extracted from WEST after the C3 (2018) and C4 (2019) campaigns, *J. Nucl. Mater.* 604 (Jan. 2025) 155525, <https://doi.org/10.1016/j.jnucmat.2024.155525>.
- [22] The ASDEX Team et al., Boronization of ASDEX, *J. Nucl. Mater.*, 176–177, (1990), pp. 350–356, doi: 10.1016/0022-3115(90)90071-T.
- [23] Q. Tichit, et al., Plasma heat load in the toroidal gaps of the ITER-like plasma facing units in WEST tokamak, *Nucl. Mater. Energy* 42 (Mar. 2025) 101899, <https://doi.org/10.1016/j.nme.2025.101899>.
- [24] H.J. Sun, et al., Impact of the plasma boundary on machine operation and the risk mitigation strategy on JET, *Nucl. Fusion* 65 (7) (June 2025) 076012, <https://doi.org/10.1088/1741-4326/addad7>.
- [25] A. Grosjean, et al., First analysis of the misaligned leading edges of ITER-like plasma facing units using a very high resolution infrared camera in WEST, *Nucl. Fusion* 60 (10) (Sept. 2020) 106020, <https://doi.org/10.1088/1741-4326/ab9fa6>.
- [26] E. Pitthan, T.T. Tran, D. Moldarev, M. Rubel, D. Primetzhofer, Influence of thermal annealing and of the substrate on sputter-deposited thin films from EUROFER97 on tungsten, *Nucl. Mater. Energy* 35 (2023) 101449, <https://doi.org/10.1016/j.nme.2023.101449>.
- [27] D. N. Gautam et al., Deuterium retention in sputter-deposited W-B layers: in-situ implantation and ion beam analysis during annealing, *Nucl. Mater. Energy*, p. 102000, Oct. 2025, doi: 10.1016/j.nme.2025.102000.
- [28] P. Ström, D. Primetzhofer, Ion beam tools for nondestructive in-situ and in-operando composition analysis and modification of materials at the Tandem Laboratory in Uppsala, *J. Instrum.* 17 (04) (Apr. 2022) P04011, <https://doi.org/10.1088/1748-0221/17/04/P04011>.
- [29] J.F. Ziegler, M.D. Ziegler, J.P. Biersack, SRIM – the stopping and range of ions in matter (2010), *Nucl. Instrum. Methods Phys. Res. Sect. B Beam Interact. Mater. at.* 268 (11) (2010) 1818–1823, <https://doi.org/10.1016/j.nimb.2010.02.091>.
- [30] J. Kotakoski, C.H. Jin, O. Lehtinen, K. Suenaga, A.V. Krasheninnikov, Electron knock-on damage in hexagonal boron nitride monolayers, *Phys. Rev. B* 82 (11) (Sept. 2010) 113404, <https://doi.org/10.1103/PhysRevB.82.113404>.
- [31] O. V. Ogorodnikova, B. Tyburska, V. Kh. Alimov, and K. Ertl, "The influence of radiation damage on the plasma-induced deuterium retention in self-implanted tungsten," *Proc. 19th Int. Conf. Plasma-Surf. Interact. Control. Fusion*, vol. 415, no. 1, Supplement, pp. S661–S666, Aug. 2011, doi: 10.1016/j.jnucmat.2010.12.012.
- [32] J. Roth, E. Tsitrone, A. Loarte, Plasma-wall interaction: Important ion induced surface processes and strategy of the EU Task Force, *Nucl. Instrum. Methods Phys. Res. Sect. B Beam Interact. Mater. at.* 258 (May 2007) 253–263, <https://doi.org/10.1016/j.nimb.2006.12.168>.
- [33] Y.-R. Lin, S.J. Zinkle, C.J. Ortiz, J.-P. Crocombette, R. Webb, R.E. Stoller, Predicting displacement damage for ion irradiation: Origin of the overestimation of vacancy production in SRIM full-cascade calculations, *Curr. Opin. Solid State Mater. Sci.* 27 (6) (Dec. 2023) 101120, <https://doi.org/10.1016/j.cossms.2023.101120>.
- [34] H. Hofäss, K. Zhang, A. Mutzke, "Simulation of ion beam sputtering with SDTrimSP, TRIDYN and SRIM," *Sel. Manusc. Aris. 18th Int. Conf. Surf. Modif. Mater. Ion Beams SMMIB-2013*, vol. 310, pp. 134–141, Aug. 2014, doi: 10.1016/j.apusc.2014.03.152.
- [35] K. Arstila et al., "Potku – New analysis software for heavy ion elastic recoil detection analysis," *11th Eur. Conf. Accel. Appl. Res. Technol.*, vol. 331, pp. 34–41, July 2014, doi: 10.1016/j.nimb.2014.02.016.
- [36] A. Schrauwen, et al., The role of composition and microstructure in Ni–W silicide formation and low temperature epitaxial NiSi<sub>2</sub> growth by premixing Si, *J. Phys. Appl. Phys.* 50 (6) (Jan. 2017) 065303, <https://doi.org/10.1088/1361-6463/aa4ed7>.
- [37] M.V. Moro, R. Holecák, L. Zendejas Medina, U. Jansson, D. Primetzhofer, Accurate high-resolution depth profiling of magnetron sputtered transition metal alloy films containing light species: A multi-method approach, *Thin Solid Films* 686 (Sept. 2019), <https://doi.org/10.1016/j.tsf.2019.137416>.
- [38] E. Pitthan, M.V. Moro, S.A. Corrêa, D. Primetzhofer, Assessing boron quantification and depth profiling of different boride materials using ion beams, *Surf. Coat. Technol.* 417 (July 2021) 127188, <https://doi.org/10.1016/j.surfcoat.2021.127188>.
- [39] A. Luukkainen, J. Keinonen, M. Erola, Density and size of neon bubbles in molybdenum, tantalum, and tantalum oxide, *Phys. Rev. B* 32 (7) (Oct. 1985) 4814–4817, <https://doi.org/10.1103/PhysRevB.32.4814>.
- [40] E. Oliviero, S. Peripolli, P.F.P. Fichtner, L. Amaral, Characterization of neon implantation damage in silicon, *Curr. Trends Nanostructured Mater. Syst.* 112 (2) (Sept. 2004) 111–115, <https://doi.org/10.1016/j.mseb.2004.05.014>.
- [41] E. Oliviero, et al., Damage accumulation in neon implanted silicon, *J. Appl. Phys.* 100 (4) (Aug. 2006) 043505, <https://doi.org/10.1063/1.2220644>.
- [42] M. Backman, N. Juslin, G. Huang, B.D. Wirth, A WNE interatomic potential for simulation of neon implantation in tungsten, *J. Nucl. Mater.* 477 (Aug. 2016) 37–41, <https://doi.org/10.1016/j.jnucmat.2016.05.002>.
- [43] T. J. Finlay, J. W. Davis, T. Schwarz-Selinger, Z. Siketić, A. A. Haasz, Deuterium retention in recrystallized tungsten irradiated with simultaneous deuterium–neon

- ion beams, Proc. 22nd Int. Conf. Plasma Surf. Interact. 2016 22nd PSI, vol. 12, pp. 1288–1293, Aug. 2017, doi: 10.1016/j.nme.2016.12.027.
- [44] A. Založnik, et al., Effect of grain size on defect annealing in displacement-damaged tungsten, Nucl. Mater. Energy 39 (June 2024) 101674, <https://doi.org/10.1016/j.nme.2024.101674>.
- [45] F. Sun, et al., Trapping and de-trapping behavior of hydrogen isotopes in <100> interstitial dislocation loops of tungsten, Nucl. Fusion 65 (7) (June 2025) 076010, <https://doi.org/10.1088/1741-4326/adda5f>.
- [46] A. Majid, A. Ali, J.J. Zhu, Y.T. Wang, Study of lattice damage produced by neon implantation into AllnN, J. Mater. Sci. Mater. Electron. 20 (3) (Mar. 2009) 230–233, <https://doi.org/10.1007/s10854-008-9708-z>.
- [47] Y. Gasparyan, et al., Helium retention in tungsten under plasma and ion beam irradiation and its impact on surface morphology, Phys. Scr. 2020 (T171) (Feb. 2020) 014017, <https://doi.org/10.1088/1402-4896/ab4068>.
- [48] Y. Gasparyan, “Quantitative characteristics of H and He interaction with radiation defects in tungsten,” presented at the 3rd Research Coordination Meeting of the CRP on “Plasma-Wall Interaction with Irradiated Tungsten and Tungsten Alloys in Fusion Devices,” Vienna, Austria, June 27, 2017. Accessed: Dec. 01, 2025. [Online]. Available: <https://amdis.iaea.org/media/presentations/F43021-RCM3-Gasparyan.pdf>.
- [49] H.T. Lee, A.A. Haasz, J.W. Davis, R.G. Macaulay-Newcombe, Hydrogen and helium trapping in tungsten under single and sequential irradiations, J. Nucl. Mater. 360 (2) (2007) 196–207, <https://doi.org/10.1016/j.jnucmat.2006.09.013>.
- [50] Y.-H. Li, H.-B. Zhou, G.-H. Lu, Towards understanding the strong trapping effects of noble gas elements on hydrogen in tungsten, Int. J. Hydrog. Energy 42 (10) (Mar. 2017) 6902–6917, <https://doi.org/10.1016/j.ijhydene.2016.12.151>.